

# Hover Performance of a Micro Air Vehicle: Rotors at Low Reynolds Number



Benjamin R. Hein\*  
Design Engineer  
Sikorsky Aircraft, Stratford, CT



Inderjit Chopra  
Alfred Gessow Professor and Director  
Alfred Gessow Rotorcraft Center  
Department of Aerospace Engineering  
University of Maryland, College Park, MD

This investigation focused on the performance of a two-bladed, micro air vehicle rotor with variations of airfoil shape and also spanwise distributions of airfoil type and twist. Rotor performance trends were studied experimentally through load measurements and flow visualization. The objective was to determine the influence of airfoil and planform variations on the hover efficiency (or figure of merit). Performance testing results showed that a micro air vehicle blade with circular arc cambered airfoil provided a large increase in the rotor efficiency, as compared to the baseline flat plate. Variation of the leading edge shape and point of maximum camber also showed improved rotor efficiency. Rotor blades with linear distribution of airfoil camber further improved the rotor efficiency over blades with uniform camber. To provide the further basis for blade variations, a laser flow visualization experiment of the rotor wake was performed. The visualization showed evidence of a highly non-ideal inflow and spanwise distribution of lift. Correspondingly, variations of spanwise twist for flat plate, cambered blades and linearly distributed airfoils revealed more optimal rotor efficiency trends. These experimental results showed gains in figure of merit that were significant across the range of non-dimensional thrust coefficients.

## Nomenclature

$A$	rotor disk area, $m^2$
$C_d$	blade section drag force coefficient
$C_l$	blade section lift force coefficient
$C_P$	rotor power coefficient, $P/\rho A(\Omega R)^2$
$C_T$	rotor thrust coefficient, $T/\rho A(\Omega R)^2$
$\bar{C}_d$	mean airfoil drag coefficient
$\bar{C}_l$	mean airfoil lift coefficient
$c$	blade airfoil chord length, m
DL	disk loading, $N/m^2$
FM	figure of merit
$h/c$	non-dimensional camber height
$N_b$	number of blades
$P$	rotor power, $Nm/s^2$
$R$	rotor radius, m
$Re$	chord Reynolds number, $\rho Vc/\mu$
$r/R$	non-dimensionalized radial distance
$T$	rotor thrust, N
$V$	flow velocity, m/s
$x/c$	non-dimensional chord station
$x_c/c$	non-dimensional chord station of maximum camber
$z/R$	non-dimensional axial wake location
$\theta_{.75}$	blade pitch at 75% blade radius, degrees

$\theta_C$	collective blade pitch, degrees
$\theta_{TW}$	non-dimensional blade twist rate, degrees
$\kappa_{ind}$	induced power factor
$\mu$	viscosity coefficient, $kg/ms$
$\rho$	air density, $kg/m^3$
$\sigma$	rotor solidity, $N_b c/\pi R$
$\psi$	wake age, degrees
$\Omega$	rotor rotational speed, 1/s

## Introduction

A micro air vehicle (MAV) is envisioned to be of small size (no dimension more than 15 cm) with weight less than 100 g and an endurance over 30 min. The primary mission of such a vehicle is to carry out surveillance in confined places. In this respect, the key characteristic of rotary-wing MAVs is their ability to hover during surveillance. To meet the endurance goal, these vehicles need to improve their hover performance.

The characteristics of rotary-wing aerodynamics in the MAV aerodynamics regime are different from those in higher Reynolds number environments. Previous studies have confirmed this fact and demonstrated that rotary-wing MAVs suffered from poor hover efficiency as compared to large-scale helicopters (Ref. 1). There are two main factors that govern the hover performance of a rotor. These are the aerodynamic profile and induced powers required to hover. The induced power of a rotor arises from the momentum change of flow generated through the rotor disk. This aspect of MAV aerodynamics was investigated in the current study and revealed the nature of a simple representative low Reynolds number rotor. The profile power generated by a rotor blade arises from two-dimensional airfoil drag, including viscous drag effects and flow

\*Corresponding author; email: bhein@sikorsky.com.

Presented at the International Specialists' Meeting Unmanned Rotorcraft: Design, Control and Testing, San Marcos Resort & Conference Center, Chandler, AZ, January 18–20, 2005. Manuscript received November 2005; accepted March 2007.

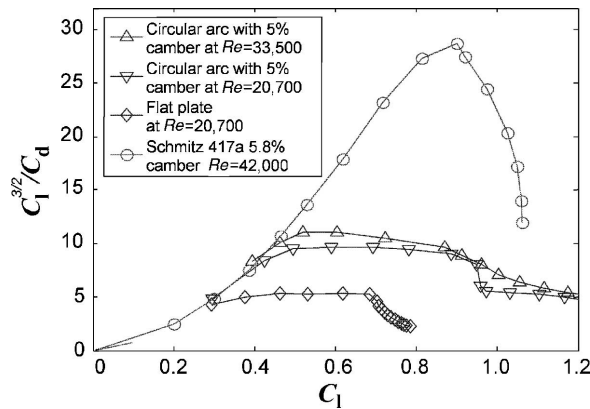


Fig. 1. Airfoil efficiency for several MAV airfoils (Refs. 2, 4).

separation drag over the airfoil. At MAV scale Reynolds numbers, typically between 10,000 and 60,000, airfoils have increased viscous drag as well as flow separation susceptibility.

As early as 1941, Schmitz examined the aerodynamics of low Reynolds number airfoils experimentally, documenting the low lift-to-drag ratios at Reynolds numbers below 100,000 (Ref. 2). Carmichael compiled a systematic survey of low Reynolds number airfoil studies, and highlighted the level of inconsistency in many experimental investigations (Ref. 3). The survey also pointed out the poor performance observed in many of these airfoils.

More recently, Laitone conducted experiments with high aspect ratio and low Reynolds number wings (Ref. 4). The tests provided reliable force coefficient data for flat plate and cambered plate wings. Flow visualization with water and aluminum particles illustrated the nature of flow around these airfoils. The data showed that flat plate and circular arc airfoils at MAV Reynolds numbers have lift-to-drag ratios that range from 5 to 13. These values are far below those of high Reynolds number airfoils, which have lift-to-drag ratios as high as 80 to 100. The study showed that high Reynolds number airfoils, such as the NACA 0012, were not suitable for very low Reynolds number environments as their measured performance showed a significant degradation at these flow conditions. It was also shown that thin plates, cambered or flat, with extremely thin leading edges (LE), exhibited characteristics less sensitive to variations in Reynolds number and turbulence at the MAV Reynolds number range. These airfoils achieved better lift-to-drag ratios than conventional airfoils. Airfoil data from these studies are presented in Fig. 1. Airfoils with a sharp leading-edge (SLE), examined at an “ultra-low” Reynolds number study performed by Sunada (Ref. 5), showed the highest lift-to-drag ratios for chord Reynolds numbers of 4000. Note that Reynolds numbers below 10,000 exist near the root end of an MAV rotor, and are therefore also of interest.

Even though Laitone’s and Schmitz’s results pointed out some of the general characteristics of MAV airfoils, they do not provide much of the key insight necessary to analytically design an efficient MAV rotor blade. To achieve more efficient rotor performance in low Reynolds number conditions, more comprehensive data of basic airfoil performance for a wide range of Reynolds numbers would be required.

MAV rotor experiments by Bohorquez and Pines (Ref. 6) have shown the critical effects of variation in camber, which are consistent with the results of the present study. In the study, the use of tapered-chord blade tips with 6% and 9% camber were used to enhance the figure of merit above the baseline rectangular blades. However, the blade design had coupled camber, thickness ratio and twist as a result of with the tapered-chord. The results of the study (Ref. 6) therefore did not differentiate between

the effects of spanwise airfoil camber distribution, solidity distribution and blade twist.

The present study was a systematic evaluation of MAV rotor performance due to variations in airfoil camber, and the effect leading edge shape. For further evaluation of planform enhancements, the same baseline blade solidity and Reynolds number distribution as well as thickness-to-chord ratio were maintained. The following results therefore isolated the effects of airfoil and twist distribution along the blade span.

### Experimental Approach

In order to better understand the hover performance trends of MAV rotors, a series of rotor parameters that affect the induced and profile power were experimentally varied in this investigation. A complete list of these parameters is provided in Table 1. The airfoil variations were compared to a baseline flat plate blade. Planform variations were compared to the 7.7% cambered airfoil blade with sharp LE as well as to the baseline flat plate blades. The hub, rotor and transmission, used for testing, can be seen in Fig. 2.

A balance that measured the thrust and torque generated by the rotor was used to determine performance data. The system used a load cell and a torque sensor. A Hall sensor was used to determine rotor rotational speed by counting dual magnet pulses per revolution. Data were recorded

Table 1. Experimental variations for MAV rotor blades

Airfoil variations		
Airfoil Camber for Circular Arc, $x_c/c = 0.5$ ( $h/c$ )	Location of $x_c/c$ for SLE Airfoil ( $x/c\%$ , $h/c\%$ )	Leading Edge Shape
4.25%	50.0%, 7.7%	Square
6.75%	45.8%, 7.4%	Sharp 15°
7.7%	36.3%, 7.5%	
9.85%		
Planform variations		
Linear Twist for Constant Airfoil, $h/c = 7.4\%$ , Root-to-Tip	Tapered Camber: Spanwise Distribution of Airfoil Camber ( $r/R$ , $h/c\%$ )	Tapered Camber: Non-linear Twist Distributions, Root-to-Tip
– 8.5°	0.00, 10.4%	– 7°
– 15.0°	0.75, 6.4%	– 9°
	1.00, 5.5%	– 13°

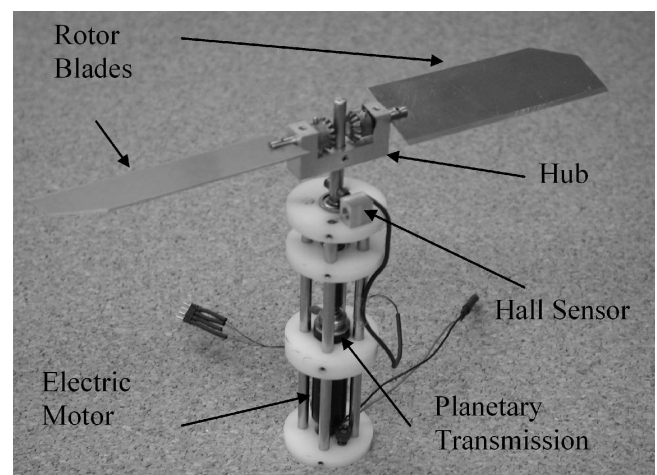


Fig. 2. Low vibration transmission and rotor assembly.

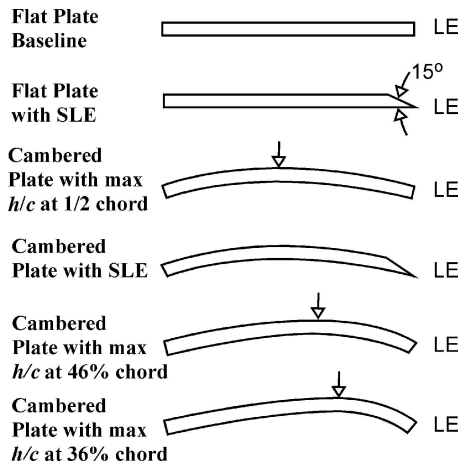


Fig. 3. Experimental airfoils shapes.

by a digital data acquisition system in conjunction with custom MATLAB software.

During testing, the rotor thrust was directed downward so that the rotor wash was propelled upward to minimize any influence due to ground effect. The thrust and torque were sampled for a test period of 10 seconds, and at a rate of 1000 samples per second. The rotor forces were found to be in steady state 8 seconds after the start of rotation. The resulting thrust data were measured to be within an accuracy of 0.0049 Newtons. The signal to noise ratio in the torque data was consistently on the order of 10:1 to 50:1. The torque cell used is rated at 10 oz-inch, accurate to within 1% and is 99.99% linear.

The baseline blade was a flat plate with square LE, as seen in Fig. 3. The blade was 20.0 mm in chord and 62.2 mm in length. The 76.2 mm blade radius rotor blades had a root cutout of 18%. The thrust weighted solidity and rotor diameter were held constant for all rotor configurations. Therefore, the chord and radius are kept constant. The blade chord and span were manufactured to a tolerance of  $\pm 1\%$ , and the values of twist were accurate to  $1^\circ$  between the root and tip of the blade. The characteristics of blades with sharp LE are also seen in Fig. 3, with a  $15^\circ$  slope on the upper surface. The sharp LE constituted about 10% of the chord length. Custom manufactured cambered blades were accurate to  $\pm 5\%$  of the nominal  $h/c$  camber thickness. All the blades used in this study were manufactured from 2024-T3 aluminum plates of 0.51 mm thickness in order to provide adequate stiffness.

To obtain a valid comparison of performance for different rotor blades, the thrust weighted rotor solidity for all the rotor blades was  $\sigma = 0.1617$ . While this solidity was higher than that of a conventional helicopter, the increased chord of the rotor blades had two important benefits. First, it reduced the thickness-to-chord ratio, and second, it increased the chord Reynolds number across the span of the blade. Both of these attributes have been shown to improve airfoil performance (Refs. 2, 4, 6).

To examine the effect of coupling between airfoil type and blade twist, three types of blades were compared. The first type employed flat plate airfoils with linear twist. The second type had nominally 7.5% camber, a sharp LE and linear twist. The twist distributions of blades with constant airfoil camber were very close to linear, and assumed to be of the form

$$\theta = \theta_{.75} + \theta_{TW}(r/R - .75). \quad (1)$$

The third type of twisted blade had a linear distribution of camber and constant chord (tapered camber), described in Table 1. The twist distributions with this type were non-linear as a result of the simplified tapered radius mold manufacturing process. For these blades, the gradient

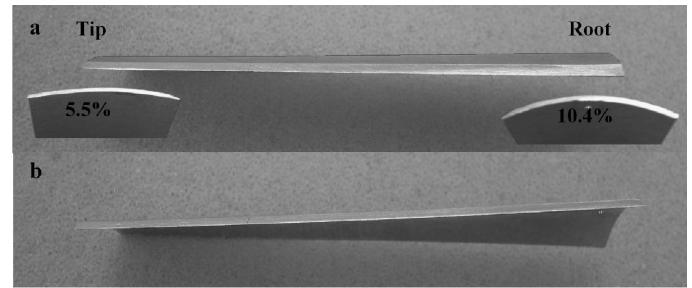


Fig. 4. (a) Root and tip cross sectional view for the untwisted tapered camber blade. (b) Leading edge view of the tapered camber blade with  $-13^\circ$  twist.

of twist was higher near the root, where the camber was larger and roughly proportional to the inverse of the radial station, as seen in Fig. 4(b). Rotor blades with such twist have more uniform disk loading distribution, which is more ideal than linearly twisted blades (Ref. 7). The comparison between blades with linear twist and the third type of twist was not strictly rigorous. However, the variation in induced power was assumed to be a second order effect.

In order to gain a better understanding of the thrust and torque results, flow visualization studies were performed. The goal of the flow visualization experiment was to reveal the structure of the MAV inflow profile. The results demonstrated some of the qualitative characteristics of the low Reynolds number rotor inflow and were used to map of the main vortex boundary. To obtain such a map, video data were taken for blade azimuth angles of  $0^\circ$ ,  $30^\circ$ ,  $90^\circ$  and  $135^\circ$ . The results from the main vortex position data were compared to Landgrebe's model (Ref. 7). Also, qualitative comments were discussed comparing the present data to full scale tail rotor shadowgraph vortex flow visualization, performed by Light (Ref. 8).

Flow visualization images were acquired by seeding the flow using a mineral oil fog, which was strobed with a laser sheet. The light sheet was produced by a dual Nd:YAG laser, which generated a light pulse on the order of nanoseconds in duration at a frequency of up to 15 Hz. The light sheet was located in the flow using an optical arm. Images were acquired using a CCD camera, and later digitized using a calibration grid. The laser and the camera were synchronized using customized electronics, which converted the rotor one-per-rev frequency into a TTL signal that pulsed every fourth rotor revolution. A phase delay was introduced so that the laser could be synchronized at any rotor phase angle.

The flow seeding is performed using a mineral oil based fluid that is broken down into a fine mist by adding nitrogen. The mist is then forced into a pressurized heater block and heated to its boiling point where it vaporizes. As the vapor escaped from the heat exchanger nozzle, it was mixed with ambient air and rapidly cools. The vapor then condensed into a fog. The fog/air mixture was passed through a series of ducts and then introduced into the rotor flow field at various strategic locations. From calibration, it was shown that 95% of the particles were between  $0.2 \mu\text{m}$  and  $0.22 \mu\text{m}$  in diameter. The mean seed particle size was small enough to minimize particle-tracking errors for the measurement of vortex positions in these experiments.

### Rotor Performance Metrics

An efficiency factor that is commonly used to compare the performance of hovering rotors of the same disk loading is known as the rotor figure of merit. The rotor figure of merit is the ratio of ideal power to actual required power of a rotor. The metric can be written in terms of

non-dimensional coefficients in the form

$$FM = \frac{C_T^{3/2}/\sqrt{2}}{C_{Pmeas}} \approx \frac{C_{Pideal}}{\kappa_{ind}C_{Pideal} + \sigma C_d/8} \quad (2)$$

Here, the ideal power is a function of thrust coefficient,  $C_T$ . The measured power,  $C_{Pmeas}$ , can be separated into induced power and profile power components. The non-ideal induced power factor is represented by the factor,  $\kappa_{ind}$ . The equation shows the profile power contribution to the required power as the second term in the denominator. The profile power is a function of rotor solidity,  $\sigma$  and the mean profile drag coefficient  $C_d$ .

For a conventional rotor, it is assumed that a  $\kappa_{ind}$  of 1.15 will cover the affects of non-uniform inflow distribution. Such a relation has not been established for MAV rotors, and may be quite different. There are also no explicit two-dimensional airfoil data for many of these airfoils in this Reynolds number range.

The definition of FM can be simplified using mean airfoil data. The  $C_T$  of the rotor can be represented as a function of the mean blade lift coefficient, shown in the approximation given below (Ref. 7).

$$\bar{C}_l = \frac{6C_T}{\sigma} \quad (3)$$

Similarly the profile power coefficient can be represented as a function of the zero lift drag coefficient (Ref. 7).

$$C_d = \frac{8C_P}{\sigma} \quad (4)$$

Substituting the mean airfoil parameters into the definition of FM in Eq. (2), the following relationship is derived.

$$FM \approx \frac{1}{\kappa_{ind} + \frac{2.6}{\sigma} \left( \frac{\bar{C}_l^{3/2}}{\bar{C}_d} \right)^{-1}} \quad (5)$$

The representation of FM in Eq. (5) is a function of an average airfoil efficiency of the blade,  $\bar{C}_l^{3/2}/\bar{C}_d$ , and the induced power factor,  $\kappa_{ind}$ . Figure 5 demonstrates how hover FM varies with  $\bar{C}_l^{3/2}/\bar{C}_d$  and  $\kappa_{ind}$ , when  $\sigma = 0.1617$ . This relationship can be better understood with the knowledge of  $\bar{C}_l^{3/2}/\bar{C}_d$  from airfoils in the MAV range, from Fig. 1. The lines of constant FM show that when  $\bar{C}_l^{3/2}/\bar{C}_d$  is below 10, as is the case of flat plate airfoils, the induced power factor has a significantly reduced effect on FM. Because of this, we expect that airfoil improvements will

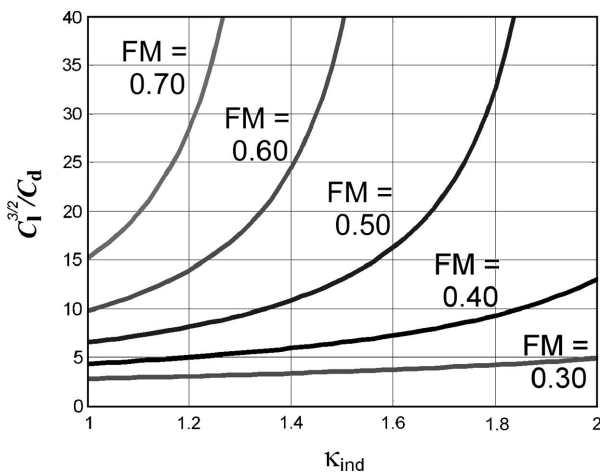


Fig. 5. The effect of induced power, airfoil selection and solidity on rotor FM (Ref. 7).

be the primary factor to influence rotor efficiency for a flat plate blade. Conversely for airfoil  $\bar{C}_l^{3/2}/\bar{C}_d$  above 10, the value of FM is increasingly more a function of induced power factor as airfoil efficiency rises. Therefore, for rotor blades with airfoils of this type, such as the cambered airfoils with sharp LE, reductions in induced power factor will yield larger increase in the rotor figure of merit compared to those with flat plate airfoils.

The key factor governing the hover performance of a rotorcraft is its power loading. Power loading is defined as the ratio of thrust to power required to hover. It can also be expressed in terms of non-dimensional variables as

$$\frac{T}{P} = \frac{C_T}{C_P} \frac{1}{\Omega R} \quad (6)$$

In dimensional terms, the power loading can be defined as a function of air density, disk loading and FM.

$$\frac{T}{P} = FM \sqrt{\frac{2\rho}{DL}} \quad (7)$$

## Results

### Airfoil performance characteristics

**Camber.** The results from the rotor experiments with variations in airfoil type showed distinct trends. Figures 6 and 7 show how the choice of airfoil affects the FM for a blade, over a range of blade loadings, for a tip chord Reynolds number of 40,900. Each airfoil tested had a circular arc with maximum camber at mid-chord. The camber is expressed in terms of blade chord, as  $h/c$ . The baseline untwisted, flat plate rotor blades had a maximum figure of merit of 0.335. The 4.25% camber blade yielded a FM of 0.472 at  $C_T/\sigma = 0.115$ . This represented a 33% increase in FM over the baseline flat plate case. Data in Fig. 6 show that an increase in airfoil camber moves the maximum FM point to a higher blade loading. The data also show that there is an optimal amount of mid-chord camber for an untwisted rotor blade. This optimum value of camber was about 6.75% of the blade chord as this airfoil produces the highest FM = 0.526. This FM value was about 48.6% higher than the baseline flat plate value. For blades with camber higher than the optimal value, such as the 7.7% camber blade, the FM was slightly reduced to a value of 0.524. Similarly, the 9.85% camber airfoil achieved a FM of 0.513.

Another interesting result in this parametric camber study was the variation of the maximum FM as a function of camber and blade loading.

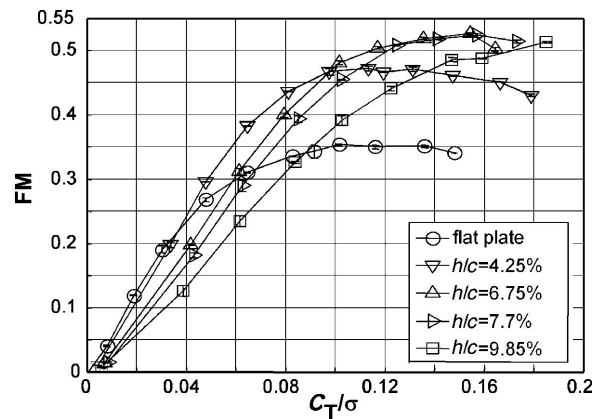


Fig. 6. Cambered airfoil performance at Reynolds number  $Re = 40,900$ .

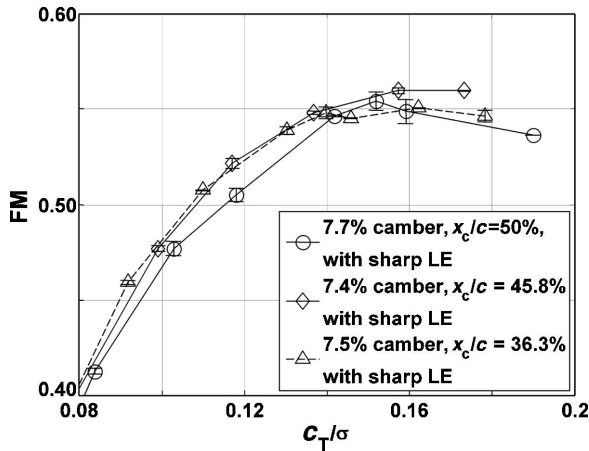


Fig. 7. The effect of shifting the maximum point of camber towards the LE for SLE airfoils, at Reynolds number  $Re = 40,900$ .

Data in Fig. 6 show how the maximum FM, at a given  $C_T/\sigma$ , corresponds to a specific amount of mid-chord camber. For  $C_T/\sigma$  less than 0.04, the flat plate blade achieved the highest FM. Between  $C_T/\sigma$  of 0.04 and 0.10, the 4.3% camber blade achieved the highest FM. This trend continued as  $C_T/\sigma$  increased, where the 6.75% camber blade had the highest FM for  $C_T/\sigma$  between 0.10 and 0.16. Between 0.16 and 0.18, the 7.7% camber blade had the highest FM. For  $C_T/\sigma$  above 0.18, the 9.85% camber blade became the most efficient. The trend showed that as blade loading increases, the amount of airfoil camber should also be increased to maintain the highest efficiency. Further, as blade loading is proportional to the mean lift coefficient across the blade span, it could be inferred that low camber airfoils were most efficient at low lift coefficients, and similarly that higher camber airfoils were most efficient at higher lift coefficients.

The data in Fig. 7 show the subtle effect of point of maximum camber for 7.7% camber airfoils. The sharp LE attribute was also present for these airfoils. From these data, the effect of location of maximum camber did not appear to be a dominating factor. For  $C_T/\sigma$  less than about 0.14, the blade with maximum camber location ( $x_c/c$ ) at 36.3% and 45.8% chord achieved a slightly higher FM than the blade with maximum camber point at mid-chord. Above  $C_T/\sigma$  of 0.14, the blade with  $x_c/c = 45.8\%$  chord achieved the highest FM. The maximum FM for the blade with maximum camber location at 36.3% was slightly lower than the maximum FM for the blade with maximum camber point at mid-chord. From these results, it appeared that the optimum point of maximum camber was ahead of mid-chord, but behind 36% chord.

**Reynolds number.** For any given airfoil, the variation of rotor FM with Reynolds number is of key importance to MAV scale rotors. To demonstrate this point, the FM for the 4.3% camber blade, as a function of rotor tip-Reynolds number, is shown in Fig. 8. There was generally a small increase in FM and  $C_T/\sigma$  as Reynolds number increased for a fixed angle of attack. The data show distinctly that the rotor efficiency had a weaker dependence on Reynolds number as compared to the amount of airfoil camber.

**Sharp leading edge airfoils.** A sharp leading edge was also found to be a significant airfoil factor. It raised the maximum FM for a flat plate as well as for a circular arc cambered airfoil, as seen in Fig. 9. By tapering the upper surface thickness at the LE (Fig. 3), two important characteristics were affected. First, the thickness ratio at the LE is lowered substantially, and second, the LE becomes slightly cambered (for the flat plate). As

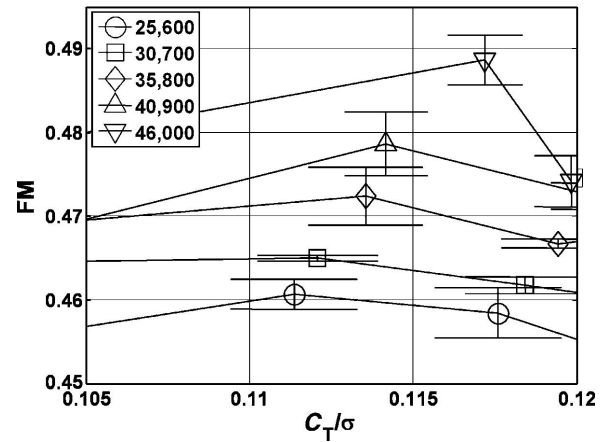


Fig. 8. MAV rotor efficiency variation with Reynolds number for 4.3% camber blade.

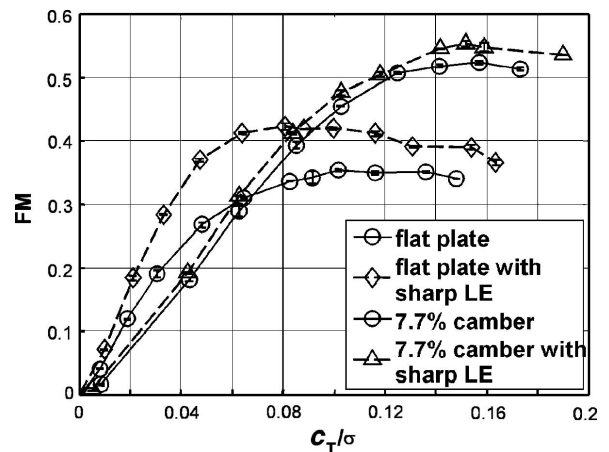


Fig. 9. The effect of sharp LE airfoils and camber distribution at  $Re = 40,900$ .

seen in Fig. 7, airfoils with maximum camber closer to the leading edge had higher airfoil efficiency. For a flat plate, this sharp LE effect raised the FM by 19% over the baseline value, even though the majority of the airfoil was unaltered. The effect of the sharp LE on the flat plate airfoil showed how important the shape and camber distribution are at the LE of an MAV airfoil. The data in Fig. 9 also show that adding the SLE to the 7.7% camber circular arc increased FM by 5.7%, a smaller effect as compared to the flat plate. The 7.7% camber airfoil with SLE yielded a maximum FM of 0.554. These results highlight the importance of LE characteristics for a low Reynolds number airfoil.

### Flow visualization

Flow visualization was performed on the 7.7% cambered blade with sharp LE (Fig. 10), using a laser sheet, in order to gain a better understanding of its flow characteristics. The visualization of the MAV rotor flow profile, with maximum FM of 0.554, showed large main vortices that extend over a large portion of the blade tip. This feature implies higher than ideal inflow velocities.

The turbulent shed vortex sheets, seen in the flow visualization, were also very thick as compared to the blade thickness. Normally, full-scale rotors have a shed vortex sheet that is very thin, and can be modeled as a discontinuity in the rotor wake (Ref. 9). The vortex sheets present

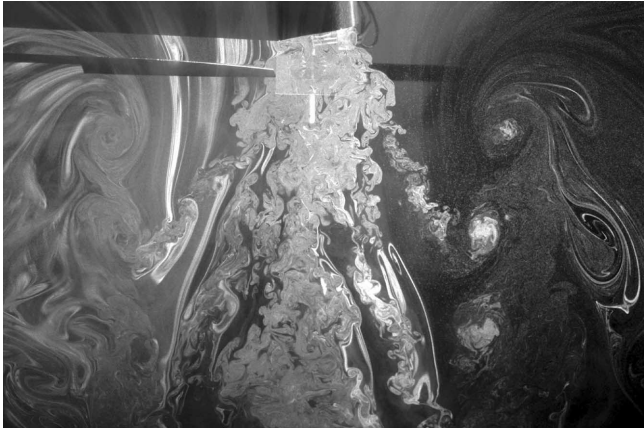


Fig. 10. Inflow at wake age of  $\psi = 30^\circ$  for a 7.7% cambered blade, 2.75% thickness with sharp LE ( $C_T/\sigma = 0.149$ ).

in the MAV rotor wake likely contributed to an induced power loss due to the energy dissipated in the flow structure. The motion of the shed wakes over time also appeared to cause another non-ideal effect. The shed wakes appeared to congregate in the root portion of the rotor wake. This phenomenon could be causing an obstruction in the axial velocity of the rotor wake.

Observations from the flow visualizations indicated a highly non-ideal inflow distribution. Normally, the wake shed from the blade remain initially bound to the main vortex generated at the tip of the blade in the early stages of formation. The wake in Fig. 10 appears to show that tip inflow affected the motion of the vortex sheet shed by the previous cycle blade. Even when the blade had traveled only  $30^\circ$  from the plane of visualization, the sheet had been rolled up into the main vortex from the preceding blade further down in the wake. In the image, it is also seen that the root portion of the shed vortex sheet had translated axially for a significantly smaller distance, as compared to the tip section shed vortex sheet. This phenomenon indicated low inflow velocities in the root. As a result, the vortex sheets rotated almost  $90^\circ$  in the far wake. This inflow profile result indicated non-uniform inflow velocities.

As predicted by blade element momentum theory, the minimum induced power for a rotor occurs when the inflow is constant across the blade span (Ref. 7). The theory also predicts that this can be achieved with an optimal blade twist distribution proportional to the inverse of the blade spanwise position. Therefore, it was expected that cambered MAV rotor blades can have lower induced power with a more uniform inflow distribution. The following performance testing results of blades with washout blade twist and cambered airfoils confirmed this hypothesis. It should be noted that results for an ideally twisted blade were not available for comparison in this experiment. Flow visualization results for an MAV rotor with ideally twisted rotor should reveal how the inflow profile and wake are affected, compared to the results for untwisted rotor. Results should indicate higher inflow in the root portion of the rotor wake and weaker tip vortices.

### Blade planform characteristics

**Blade twist.** Hovering rotor blades are typically designed with washout twist to increase the lift coefficient of the inboard portions of the blade to create a more even inflow distribution across the blade span. Ideally, an inflow distribution with less spanwise variation will reduce the induced power factor, leading to higher FM. Initially, blades with flat plate airfoils were twisted, to study the parametric effect on FM. In Fig. 11, the

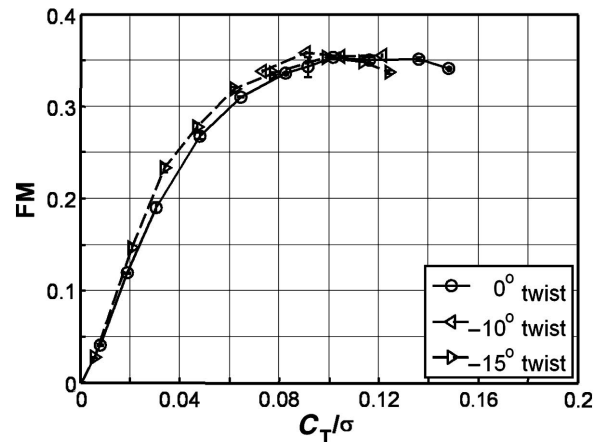


Fig. 11. Performance of blade with flat plate airfoil, square LE and with washout twist at Reynolds number  $Re = 40,900$ .

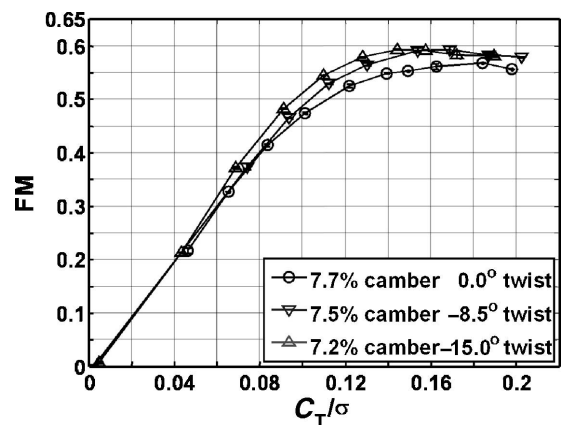


Fig. 12. Performance enhancements for nominally 7.5% camber airfoils and SLE with linear twist at Reynolds number  $Re = 40,900$ .

$-10^\circ$  twisted flat plate blade FM distribution showed that only a small increase in maximum FM occurs over the baseline untwisted blades at  $C_T/\sigma = 0.09$ . However, at lower blade loadings for both the  $-10^\circ$  and  $-15^\circ$  twisted blades, an increase in FM by 2–4% was observed, over the baseline.

Results for the rotor blades with nominally 7.5% camber, sharp LE airfoil (with maximum camber at mid-chord), and linear twist are seen in Fig. 12. The figure indicates a significant benefit in FM due to twist, compared to the baseline. Each blade with airfoil camber and linear twist achieved an increase in FM over the full range of experimental blade loadings. At blade loadings below the point of maximum FM, the  $-15^\circ$  twisted blades had higher FM than the less twisted  $-8.5^\circ$  blade. For a blade loading of 0.144, the  $-15^\circ$  twisted blades FM was 8% higher than the untwisted cambered blades, and the  $-8.5^\circ$  twisted blade FM was 5% higher. The efficiency of both twisted blade rotors appears to converge to roughly the same value for blade loadings at, and also higher than, the point of maximum FM. Both twisted rotor blade sets achieved a maximum FM of 0.593. The maximum FM of the  $-15^\circ$  twisted blade was roughly 4% higher than that of the untwisted 7.7% camber blades with SLE, and occurred at a lower blade loading.

**Tapered camber and twist.** An uneven distribution of inflow was observed in the flow visualization for the untwisted 7.7% camber blade rotor. This phenomenon contributed to higher induced power, as thrust

is more concentrated near the blade tips, which produced lower FM. To correct this problem, knowledge gained from the previous airfoil results was used to design a more efficient blade.

As discussed, the blade element-momentum theory predicts that optimum twist should produce uniform inflow across the blade span, resulting in the minimum induced power. The theory also predicts that the optimum taper distribution for a rotor blade is inversely proportional to the chord length at the blade tip (Ref. 7). When the blade is designed with an optimum twist distribution, optimum taper provides a uniform lift distribution because the angle of attack at all blade sections also becomes uniform. Proper blade design for a hovering rotor will chose the solidity such that the angle of attack corresponds to the highest lift-to-drag ratio to give the minimum profile power.

Previously, it was shown that blades with flat plate airfoil and tapered-chord did not significantly increase the rotor FM (Ref. 10). Blade designs with cambered airfoils and tapered-chord at the tip showed improved FM, however the design reduced the Reynolds number and increased the thickness-to-chord ratio at the blade tip, as in a previous study (Ref. 6). The data in Fig. 8 show how efficiency was adversely affected as Reynolds number was decreased. Therefore, it was desired to optimize the lift-to-drag ratio while maintaining the baseline Reynolds number distribution by varying the spanwise airfoil camber distribution.

For an untapered and twisted blade the local lift coefficient required for uniform inflow rises as the section approaches the root from the tip (Ref. 7). Figure 6 shows the relationship between optimum airfoil camber and blade loading, or equivalently, optimum airfoil camber and lift coefficient, for airfoils used in this study. The data show that the value of camber, for highest efficiency, rises with mean lift coefficient. Therefore, a twisted blade with higher camber in the root sections and lower camber near the tip should have higher efficiency than a blade with constant camber airfoil sections.

To confirm the relationship between camber and lift coefficient, blades with a linear distribution in camber were designed and tested for a range blade twist from  $0^\circ$  to  $-13^\circ$ , as measured from root to tip. These blades had a linear distribution of camber (tapered camber) across the blade span, with 10.4% camber at the start of the root cutout (18% radius), 6.4% camber at the 75% radius location, and 5.5% camber at the tip. The precise characteristics of the tapered camber blade are presented in Table 1, and Fig. 4(a).

Performance results of the untwisted tapered camber blade are seen in Fig. 13. This blade type produced higher rotor FM at all blade loadings, with maximum FM = 0.574, compared to the constant 7.7% camber blade

(FM = 0.568). The tapered camber blade showed that the redistribution of airfoil type increases the blade efficiency. The tapered camber blades benefited from an initial redistribution of lift. Even without twist, the higher cambered airfoils, near the root, have higher lift coefficients for a given angle of attack than lower camber airfoil sections, as the zero-lift angle of attack is typically shifted to negative angle-of-attack. The reduced airfoil camber near the tip reduced the blade tip contribution to thrust for the same reason.

Figure 13 also shows the results for blades with tapered camber for several twist distributions. The data show that the FM, for the rotors with twisted and tapered camber blades, was greater than the untwisted rotor, for all blade loadings. For the rotor with tapered camber blade and with the greatest degree of twist, 26.6% and 21.0% gains in FM were seen at blade loadings of 0.066 and 0.101 respectively, as compared to the untwisted tapered camber blade. The maximum figures of merit were 0.598, 0.609, and 0.622, respectively, with the  $-7^\circ$ ,  $-9^\circ$  and  $-13^\circ$  twisted blades. These results showed that the overall FM rose for all values of blade loading when both the profile and planform parameters were simultaneously improved.

*Profile and planform parameter coupling.* It is theorized (Eq. (5)) that the FM of rotors with higher mean airfoil efficiency ( $\bar{C}_l^{3/2}/\bar{C}_d$ ) benefited more from planform enhancements that reduced induced power. Three levels of airfoil efficiency were observed in the present study. First, it was shown in the literature, as well as by the original airfoil parameter variations (Fig. 6), that the airfoil efficiency of higher camber blades with SLE was greater than flat plates (Refs. 4, 5, 9). Second, it is shown in Fig. 13 that the untwisted tapered camber blade achieved a higher FM compared to the blade with uniform camber, suggesting higher mean airfoil efficiency. The increasing improvement in maximum FM and FM distribution in the results for twisted blades with increasingly efficient airfoil distribution reveals that the trend illustrated in Fig. 5 is experimentally valid for MAV rotors.

*Power loading.* The power loading, or thrust efficiency, is defined as thrust generation per unit power. It was important to see how the knowledge of FM governed the power loading for an MAV rotor. Figure 14 shows a plot of the power loading as a function of disk loading for a range of rotational speeds. Each data curve represented the rotor at the same  $\Omega$ , measured in revolutions per minute (RPM), for a range of collective angles. The blade with 7.7% camber and sharp LE were chosen to present these results.

Figure 14 shows that, at any disk loading, there was a specific combination of collective angle and rotational speed corresponding to the maximum power loading. By correlating information from the FM vs.  $C_T/\sigma$  plots (Fig. 9), it was discovered that the  $C_T/\sigma$  for maximum thrust efficiency at any disk loading also corresponded to the  $C_T/\sigma$  for the highest FM for that rotational speed. This indicated that for any given blade and thrust level, the most efficient operation occurred at a constant blade pitch where FM was a maximum. Hence, for an optimally efficient rotor, rotational speed should be variable, which is a viable option for rotary-wing MAVs. Figure 15 shows a comparison of power loadings between the flat plate blade with sharp LE, the 7.7% camber blade with sharp LE, and the tapered camber blade with  $-9^\circ$  twist, at the constant blade loading where FM was maximum. The higher FM achieved by the cambered airfoil shifted the curve upward to higher power loading for all disk loading. The tapered camber blade was observed to have a power loading 39% higher than the flat plate with SLE and 10% higher than the 7.7% camber blades, for a disk loading of 0.4 lb/ft<sup>2</sup>.

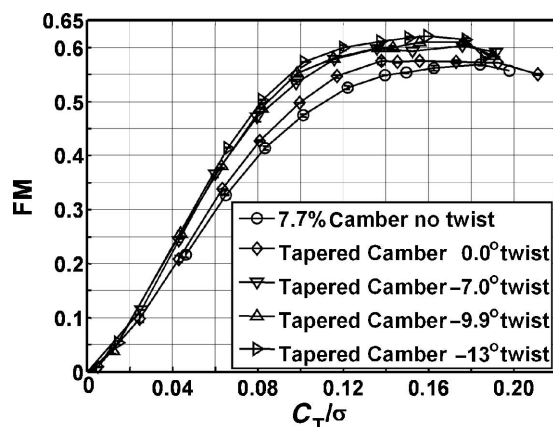


Fig. 13. Performance enhancements from tapered camber distribution with twist at Reynolds number  $Re = 40,900$ .

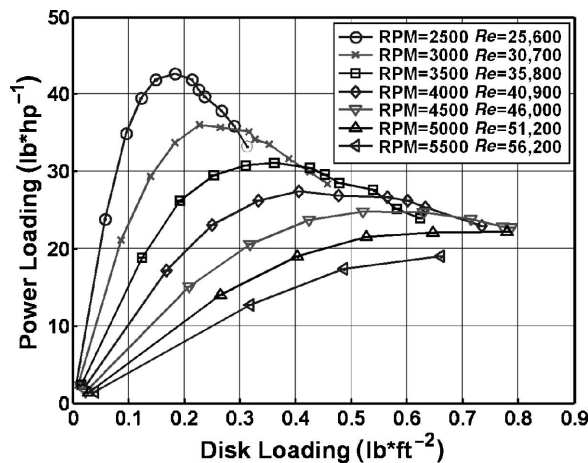


Fig. 14. Power loading as a function of disk loading for the 7.7% camber SLE blade.

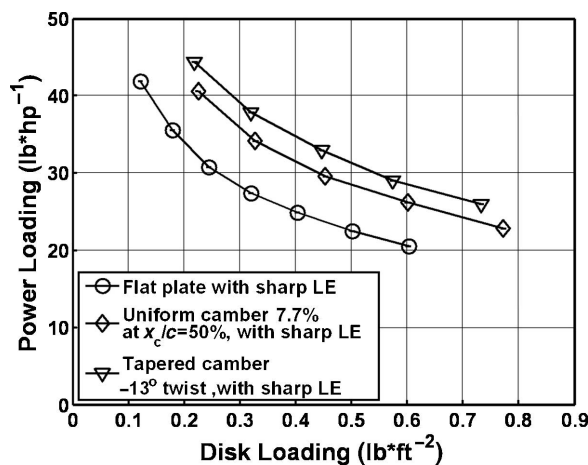


Fig. 15. Power loading at maximum FM blade collective pitch angle.

#### Vortex mapping of flow visualization

An analysis of the locations of the main vortex cores can be seen in Fig. 16. The locations of the vortex cores identified the boundary of the rotor slipstream. These data were collected from a rotor at  $C_T/\sigma = 0.149$  with FM of 0.554, using the blades with 7.7% camber and a sharp LE. Each cluster of data in Fig. 16 represents the location of a vortex core at the indicated wake age. The wake age of a vortex indicated how many degrees of rotation the blade had traveled out of the plane of visualization. These data show up to three coherent vortex centers for any given azimuth angle. Since a two-bladed rotor was used in this investigation, the second and third vortex images represented the 180° and 360° blade vortices.

The data in Fig. 16 show that the motion of the main vortex cores as they were conducted into the rotor wake. After one rotor revolution, the positions of vortex cores had nearly contracted asymptotically to half the rotor disk area, or  $r/R = 0.7$ . This result was unlike the larger scale rotor case where  $r/R$  approaches 0.78 (Ref. 7). Moreover, with the previously mentioned obstruction present in the root portions of the far wake, the total area available for axial flow would be significantly reduced below the value predicted by momentum theory. This phenomenon would be similar to a converging duct causing increased induced velocities in the far wake. It was also highly unusual to observe that the  $\psi = 0^\circ$  vortex was above the

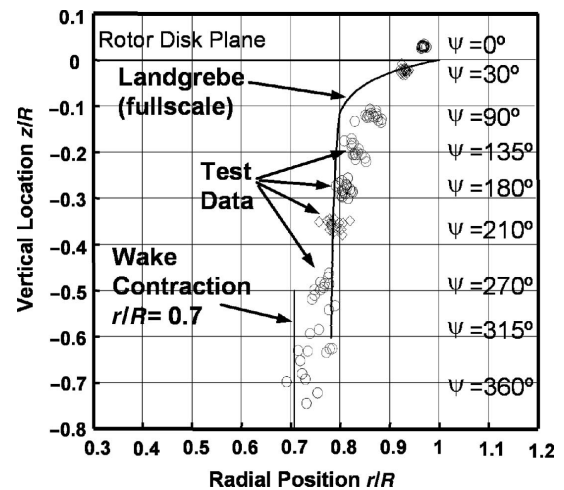
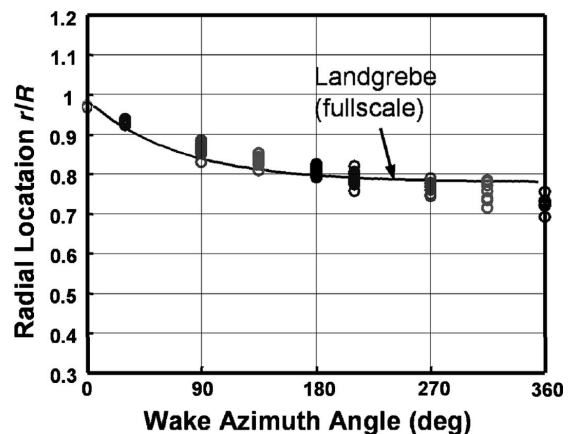
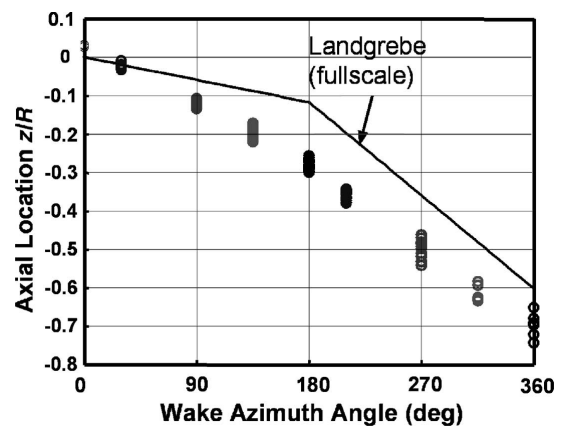


Fig. 16. Measurements of tip vortex core location over one rotor revolution.



(a)



(b)

Fig. 17. Measurements of tip vortex core axial position and radial position with respect to wake age.

tip path plane of the rotor. This observation indicated unusually strong tip vortices. These phenomena were indications of highly non-ideal inflow velocity distributions, as previously discussed. The effects manifested as lower figure of merit because of higher effective disk loading and therefore lower efficiency for a given rotor diameter.

Included in Figs. 16 and 17 was Landgrebe's empirical formulation for the hovering wake model (Ref. 7). A comparison of the model with



the data collected from the flow visualization showed some differences between the model and the axial and radial position data of the tip vortex motion. In Fig. 17, the radial and axial locations of the tip vortex locations were shown as a function of wake age. Correlating the data for radial location with Landgrebe's model showed a good approximation before a wake age of  $180^\circ$ . For greater wake ages, a slightly larger contraction ratio was seen in the far wake than the prescribed  $r/R = 0.78$ , as previously noted. The Landgrebe model also under-predicted the axial rate of convection, with respect to wake age, of the main vortices into the far wake. This result concurred with the previous observation that the axial wake velocity in the tip region was higher than the average velocity, seen from Fig. 10.

The data in Fig. 16 show increasing radial and axial scatter of the location of the vortex center as wake age increases. This was primarily attributed to unsteady motion of the vortex core observed in the flow visualization video data. However, this unsteady motion could not be fully attributed to the rotor blade aerodynamics, as the flow visualization environment did not control the ambient conditions of air in the near and far fields. However, shadowgraph flow visualization data of a full scale tail rotor wake, performed outdoors by Light (Ref. 8), showed that the axial and radial vortex locations do not show strong unsteadiness until after  $\psi = 270^\circ$ . The MAV data showed increased scatter as early as  $30^\circ$  wake age, and increasing scatter with increasing wake age. This observation indicated a larger degree of unsteadiness in the MAV rotor wake compared to larger scale rotors.

### Conclusions

1) In this study, cambered blades with maximum camber ahead of the mid-chord, and sharp LE blades exhibited the best airfoil characteristics, resulting in high rotor figure of merit in hover.

2) Results showed that an optimum airfoil camber is about 6.75% of the chord. Rotors blade airfoils with higher values of camber result in reduced maximum FM.

3) Airfoil variations of thin MAV rotor blades showed that the optimum amount of camber, with respect to the chord, rises as a function of mean lift coefficient.

4) Planform parameter variations that optimized camber and twist distribution successfully raised the efficiency by reducing the profile and induced power of the rotor. These results are verified by the tapered camber blade experiments that include both twisted and untwisted blades. The rise of maximum FM from the flat plate, to the twisted constant camber blades, to the tapered camber twisted blades showed that the FM of rotors with higher mean airfoil efficiency benefit more from planform enhancements.

5) Flow structures seen from flow visualization of an untwisted rotor blade show a turbulent vortex region that arises from the congregation of

shed vortex sheets. The data also show a non-uniform inflow distribution with a lower axial velocity near the root section of the wake. This results in low figure of merit seen by MAVs. The flow visualization study also showed a larger degree of main vortex motion unsteadiness as compared to full-scale flow visualization studies.

### Acknowledgments

This research work was supported by the Army Research Office under the MAV MURI Program (ARMY-W911NF0410176) with Dr. Gary Anderson as Technical Monitor. The authors thank Dr. M. Ramasamy and Dr. J. Gordon Leishman for their assistance with the flow visualization experiments. The authors also thank Dr. J. Sirohi and F. Bohorquez for their advice and support with these experiments.

### References

- <sup>1</sup>Bohorquez, F., Samuel, P., Sirohi, J., Pines, D., Rudd, L., and Perel, R., "Design Analysis and Hover Performance of a Rotary Wing Micro Air Vehicle," *Journal of the American Helicopter Society*, Vol. 48, (2), April 2003, pp. 80–90.
- <sup>2</sup>Schmitz, F. W., *Aerodynamics of the Model Airplane (1941)*, Redstone Arsenal, N70-39001, RSIC-721, November 1967.
- <sup>3</sup>Carmichael, B. H., "Low Reynolds Number Airfoil Survey," NASA Contractor Report 165803, Vol. I, 1981.
- <sup>4</sup>Laitone, E. V., "Wind Tunnel Tests of Wings at Reynolds Numbers Below 70,000," *Experiments in Fluids*, Vol. 23, 1997, pp. 405–409.
- <sup>5</sup>Sunada, S., "Comparison of Wings Characteristics at an Ultralow Reynolds Number," *Journal of Aircraft*, Vol. 39, (2), March–April 2000, pp. 331–337.
- <sup>6</sup>Bohorquez, F., and Pines, D., "Rotor and Airfoil Design for Efficient Rotary Wing Micro Air Vehicle," American Helicopter Society 61st Annual Forum Proceedings, Grapevine, TX, June 1–3, 2005.
- <sup>7</sup>Leishman, J. G., *Principles of Helicopter Aerodynamics*, Cambridge University Press, New York, 2002, Chap. 2 and 3.
- <sup>8</sup>Light, J. S., "Tip Vortex Geometry of a Hovering Helicopter Rotor in Ground Effect," American Helicopter Society 45th Annual Forum Proceedings, Boston, MA, May 22–24, 1989.
- <sup>9</sup>Martin, P. B., and Leishman, J. G., "Trailing Vortex Measurements in the Wake of a Hovering Rotor Blade with Various Tip Shapes," *Journal of the American Helicopter Society*, Vol. 48, (1), January 2003, pp. 39–52.
- <sup>10</sup>Hein, B., and Chopra, I., "The Hover Performance of a Micro Air Vehicle: Rotors at Low Reynolds Numbers," American Helicopter Society International Specialists' Meeting Unmanned Rotorcraft: Design, Control and Testing, Phoenix, AZ, January 18–20, 2005.